



Design, modelling and system level simulations of DRIE-based MEMS differential capacitive accelerometer

R. Mukhiya^{1,2} · P. Agarwal³ · S. Badjatya³ · M. Garg⁴ · P. Gaikwad¹ · S. Sinha^{1,2} · A. K. Singh⁴ · R. Gopal¹

Received: 14 October 2018 / Accepted: 31 December 2018 / Published online: 10 January 2019
© Springer-Verlag GmbH Germany, part of Springer Nature 2019

Abstract

The paper presents design, analytical modelling and system level simulations of a highly sensitive single-axis in-plane Micro-Electro-Mechanical-Systems (MEMS) differential capacitive accelerometer. The designed accelerometer is Deep-Reactive-Ion-Etching (DRIE)-based with Silicon-on-Insulator (SOI) wafer technology. Analytical models have been derived for frequency as well as transient response analysis. For system level simulations, accelerometer model were extracted from MEMS+[®] and further integration for the readout electronics were performed using MATLAB Simulink[®] module. The accelerometer has response time of 0.7 ms and settling time of 5 ms. The accelerometer has the displacement sensitivity of 0.121 $\mu\text{m/g}$, capacitive sensitivity of 225 fF/g and electrical sensitivity of 0.34 V/g for MS3110 capacitive to voltage readout circuitry, with a resolution of better than 1 mg. The device shows very less non-linearity ($\sim 0.3\%$) in the operating range of ± 5 g with a bandwidth of 100 Hz. The simulation results of designed open-loop readout circuitry to read the applied acceleration in terms of voltage are also presented.

1 Introduction

With the growing market and numerous ranges of applications, MEMS inertial sensors have become an integral part of many systems such as smartphones, air-bag deployment, and navigation and control in aerospace applications (Finkbeiner 2013). Predominantly, piezoelectric, piezoresistive and capacitive transduction mechanisms are used for various sensing applications. Capacitive technique offers several advantages such as less sensitivity to temperature and noise, high linearity, low power dissipation and ease of readout circuitry (Mukhiya et al. 2015; Yazdi et al. 1998). Half-bridge and differential topologies

are popularly used for readout operations. Differential topology provides the advantage of increased sensitivity (Yazicioglu 2003).

In the earlier reported accelerometers, there is a trade-off between bandwidth and sensitivity. In particular, (Sinha et al. 2014) reported a sensitivity of 3.83 fF/g with a bandwidth of 400 Hz. However, in this paper, a sensitivity of 225 fF/g with a bandwidth of 100 Hz is achieved while overwhelming the trade-off by designing smaller capacitive gaps and large number of combs.

Monolithic integration of MEMS structure with CMOS technology is an important feature in modern day accelerometers, ensuring high performance, miniaturization, high resolution and low power consumption (Qu 2006). Silicon on Insulator (SOI) based MEMS sensor have become irresistible over the past few years, because of their compatibility with monolithic integration (Mistry et al. 2010). The accelerometer structure presented in this paper can be fabricated using Deep Reactive Ion Etching (DRIE) and post CMOS-MEMS technology, providing improved mechanical and electrical performance using SOI wafer. The achievement of high quality etch profile using DRIE is the major reason for its usage in high performance accelerometers (Senturia 2001). The increased number and overlap area of the sensing fingers ensures the larger

✉ R. Mukhiya
rmukhiya@ceeri.res.in

¹ Smart Sensors Area, CSIR-Central Electronics Engineering Research Institute (CEERI), Pilani 333031, India

² Academy of Scientific and Innovative Research (AcSIR), Chennai 600113, India

³ Department of Mechanical Engineering, BITS-Pilani, K.K. Birla Goa Campus, Goa 403726, India

⁴ Department of Electronics and Communication Engineering, Punjab Engineering College (Deemed to be University), Chandigarh 160012, India

capacitive sensitivity and the gap between sensing fingers can be realised using DRIE process.

SOI wafers provide better mechanical and electrical performance, robustness and lower parasitics due to effective isolation of active and bulk layers. Moreover, they are also compatible with DRIE process. DRIE-based process is preferred over other techniques, viz.; surface micromachining, LIGA process and wet micromachining; because DRIE-SOI process has better performance and good control on the high-aspect-ratio (HAR) structure geometry (Mistry et al. 2010; Bais and Majlis 2008). In surface micromachining, poly-silicon is used as the structural material, which has thickness of around 2–5 μm which limits the change in capacitance (Sinha et al. 2014; Bais and Majlis 2008) and requires CMOS-MEMS on-chip integration. This CMOS-MEMS integration makes the process very complex and is also not available at the authors' laboratory. In LIGA processes, the material used is metal (Ni/Ni-Fe). These can have fatigue issues when compared to the silicon (Sinha et al. 2014; Van Spengen 2003). Using wet bulk-micromachining processes, it is difficult to realize the HAR structure with vertical side walls; hence it is not considered as the proposed process. SOI wafer used in our case is wafer bonded and it is important to consider the residual stress while performing simulations and in the mathematical modelling. However, in the presented work we have not considered the effect of residual stress.

In this paper, MEMS capacitive accelerometer based on the differential topology is designed and simulated using MEMS+[®] tool. MEMS+[®] provides accuracy and speed in comparison to other tools such as CoventorWare[®]. The 3D model is designed and simulated using MEMS+[®] which is imported to MATLAB Simulink[®] to carry out system level simulations.

The read out circuitry to read the applied acceleration in terms of voltage is capable of handling capacitance changes in the range of ± 1.14 pF. The full scale output ranges from 0.5 to 4 V for the acceleration range of ± 5 g. The accelerometer gives an output of 2.288 V for 0 'g' acceleration.

The paper is organised in the following manner: Sect. 2 introduces the structure and analytical calculations of capacitive accelerometer. Section 3 presents the simulation results of 3D model structured in MEMS+[®], Sect. 4 presents the simulation results of designed open loop readout circuitry, Sect. 5 presents results and discussions, Sect. 6 compares analytical results and simulated results and Sect. 7 presents conclusions.

2 Accelerometer structure and design

DRIE-based MEMS differential capacitive accelerometer is designed and simulated using MEMS+[®] and MATLAB Simulink[®]. The schematic of the accelerometer along with biasing is shown in Fig. 1.

The movable proofmass is suspended via springs connected to the anchor. The stator fingers connected to the anchor are fixed. Figure 2 shows the DRIE-based 3D solid model of the accelerometer designed in Coventor Ware[®] using SOI wafer with the specifications mentioned in Table 1.

Working principle of the accelerometer can be understood by the conventional spring, mass and damper system. The mass is called as seismic mass or proofmass. Under the application of external acceleration, the proofmass displaces from its original position and according to Newton's second law of motion, all the forces acting on the proofmass are equal to the inertial force acting on the proofmass. Hence, accelerometer can be modelled by second order differential Eq. (1), provided no biasing is applied to the electrodes (Kannan 2008).

$$F_{\text{applied}} = m\ddot{x} + F_{\text{damper}} + F_{\text{spring}} \quad (1)$$

$$F_{\text{applied}} = m\ddot{x} + b\dot{x} + kx = ma, \quad (2)$$

where, m is the proofmass, b is the damping coefficient, k is the spring constant and a is applied acceleration.

Taking Laplace transform we get,

$$a(s) = \left(s^2 + \frac{b}{m}s + \frac{k}{m}\right)x(s) \quad (3)$$

$$\frac{x(s)}{a(s)} = \frac{1}{\left(s^2 + \frac{b}{m}s + \frac{k}{m}\right)}. \quad (4)$$

Comparing (4) with

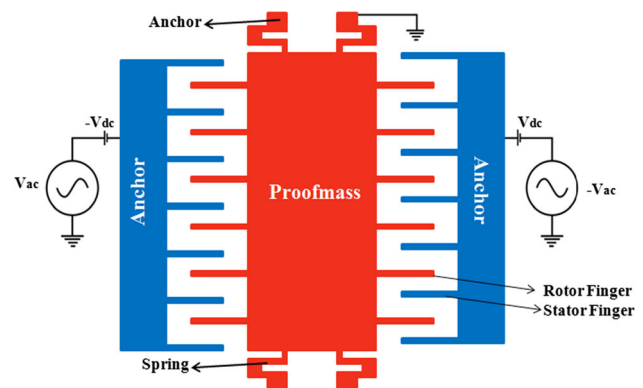


Fig. 1 Schematic of MEMS differential capacitive accelerometer

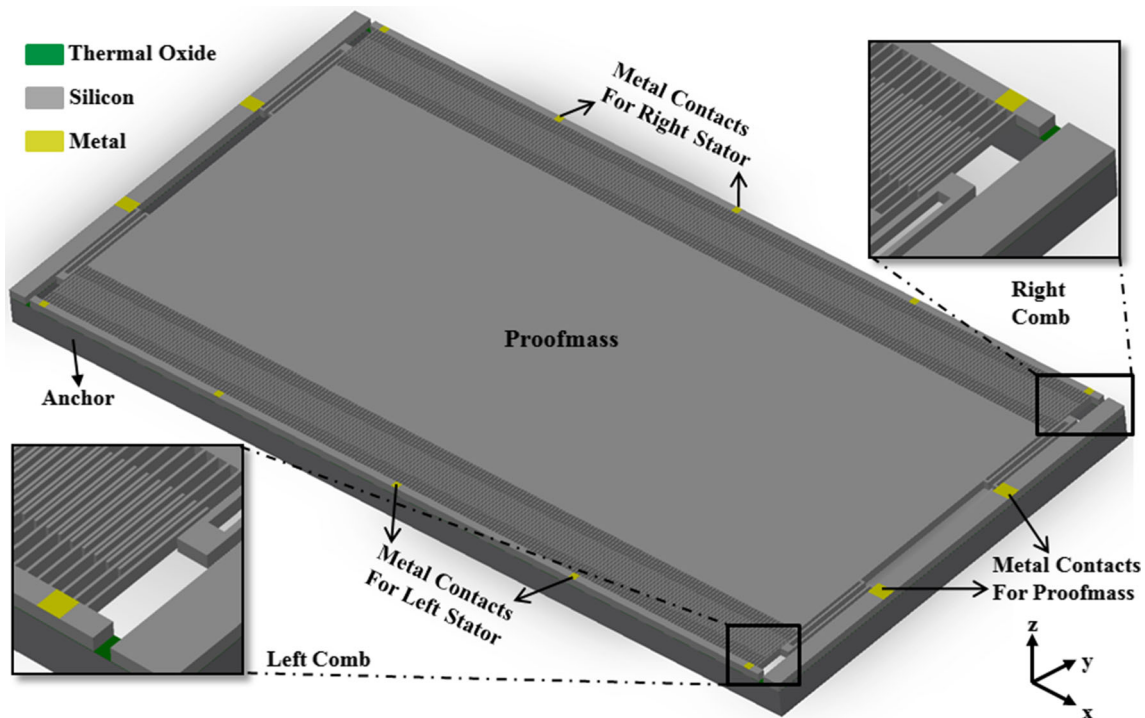


Fig. 2 DRIE-based 3D solid model of the accelerometer

Table 1 SOI wafer specifications

Parameter	SOI wafer
Size (inches)	3-Inch
Orientation	Si <100>
Device/active layer	Silicon
Thickness	30 ± 1 μm
Dopant/type	Antimony/n-type
Resistivity (Ω-cm)	0.01–0.05
Bow	< 10 μm
Surface roughness	20 Å
Buried layer	Oxide (thermally grown)
Thickness	1 μm
Bulk/handle layer	Silicon
Thickness	400 ± 10 μm
Dopant/type	Phosphorus/n-type
Resistivity (Ω-cm)	1–10
Bow	< 10 μm
Surface roughness	20 Å

$$T(s) = \frac{1}{(s^2 + 2\zeta\omega_n s + \omega_n^2)},$$

we get,

$$\omega_n = \sqrt{\frac{k}{m}} \Rightarrow f_n = \frac{1}{2\pi} \sqrt{\frac{k}{m}} \quad (5)$$

$$2\zeta\omega_n = \frac{b}{m} \Rightarrow \zeta = \frac{b \cdot \sqrt{km}}{2}, \quad (6)$$

where, ω_n is the natural frequency in rad/s, f_n is the natural frequency in Hz and ζ is the damping factor/ratio.

Under static response ($\omega = 0$)

$$\frac{x}{a} = \frac{m}{k}. \quad (7)$$

Using (5 and 7), we get

$$x = \frac{a}{\omega_n^2}. \quad (8)$$

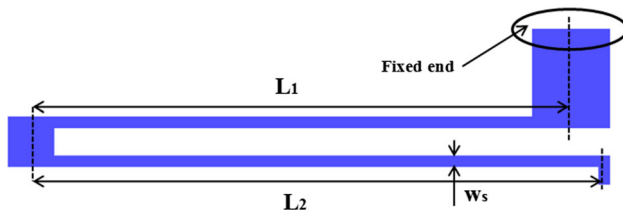
Accelerometer is designed as per the specifications mentioned in Table 2.

2.1 Spring structure

Mechanical spring stiffness (k) is an important element in second order differential Eq. (2). The spring structure (Fig. 3) is considered a linear model with Bernoulli beam element type for fast and accurate simulation. In this element type, stress along beam axis is significant but it is negligible along cross-axis, based on Euler–Bernoulli beam theory. The gap between two parallel beams is more than three times the maximum displacement of structure to accommodate mechanical force, electrical force and

Table 2 Initial design considerations

Parameter	Value
Device thickness (t)	30 μm
Resolution (a_{\min})	1 mg
Electrical noise (ENEA)	5 aF/ $\sqrt{\text{Hz}}$
Natural frequency (f_n)	1.5 kHz
Operating bandwidth	100 Hz
Maximum operating temperature	80 $^{\circ}\text{C}$
Operating range	± 5 g
Differential capacitance for 1 g	150–200 fF

**Fig. 3** Spring structure

thermal expansion. Anchors are large to hold structure in its place. Relationship between the spring constant, spring length and spring width with series and parallel combination of beam elements is given by:

$$k = 2 \left(\frac{\pi^4}{6} \left(\frac{E \cdot t \cdot w_s^3}{(2 \cdot L_1)^3 + (2 \cdot L_2)^3} \right) \right), \quad (9)$$

where, E is Young's modulus, w_s is the width of beam, L_1 and L_2 are the lengths of beam, and t is the thickness. Here, we have kept $L_1 = L_2 = L_s$ to calculate spring constant. The dimensions of the anchor and the small beam joining the two longer beams do not affect the value of spring constant significantly and are considered as nearly rigid (Senturia 2001).

2.2 Noise calculations and sensitivity

The total noise contributed by the two major sources of noise; electrical noise equivalent acceleration (ENEA) and mechanical noise equivalent acceleration (MNEA) is given by the Eq. (10) as mentioned in (Freescall Semiconductor 2007).

$$\text{Noise}_{\text{total}} = \frac{\sqrt{\text{ENEA}^2 + \text{MNEA}^2}}{\sqrt{1.6 \times \text{bandwidth}}}. \quad (10)$$

MNEA is $< 1\%$ of ENEA, and therefore MNEA is ignored, while calculating total noise. For a high signal to noise (SNR) ratio, the signal which is differential change in capacitance in capacitive accelerometers, should be at least

three times the total noise. Hence the sensitivity (S) can be calculated as the ratio of differential change in capacitance and resolution as stated in Eq. (11).

$$S = \frac{\text{Differential Change in Capacitance}}{\text{Resolution}} = \frac{3 \times \text{Noise}_{\text{total}}}{\text{Resolution}}. \quad (11)$$

Using Eq. (8) for a minimum change in displacement (x_{\min}), acceleration should be minimum (a_{\min}), therefore

$$x_{\min} = \frac{a_{\min}}{\omega_n^2}. \quad (12)$$

2.3 Physical dimensions

Figure 4 shows the schematic of the comb structure. Gap $d_1 = 3.5 \mu\text{m}$ selected to meet the fabrication feasibility aspects. The ratio $\frac{d_2}{d_1} = 3$, has been selected to provide maximum change in capacitance. The minimum number of combs required to produce x_{\min} can be calculated by the Eq. (13b) as mentioned in (Edalatfar et al. 2016).

$$\Delta C = \frac{2 \cdot \epsilon \cdot l \cdot t \cdot N \cdot (d_2^2 - d_1^2) \cdot x_{\min}}{(d_1^2 - x_{\min}^2)(d_2^2 - x_{\min}^2)}, \quad (13a)$$

$$N = \frac{\Delta C \cdot (d_1^2 - x_{\min}^2) \cdot (d_2^2 - x_{\min}^2)}{2 \cdot \epsilon \cdot l \cdot t \cdot (d_2^2 - d_1^2) \cdot x_{\min}}, \quad (13b)$$

where, ϵ is permittivity of air, l is the overlap length of combs, t is the thickness, N is the number of combs, d_1 is the smaller gap between electrodes, d_2 is the larger gap between electrodes.

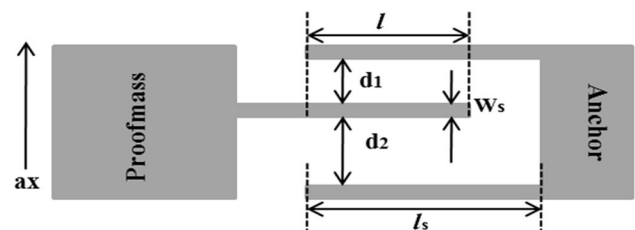
Now, minimum length (l_m) of the proofmass required to accommodate N number of combs can be calculated as

$$l_m = (d_2 + d_1 + 2 \cdot w_c) \times N - (d_2 + d_1 + w_c), \quad (14)$$

where, w_c is the comb width.

While designing the structure of proofmass, an aspect ratio of 2.5 has been selected to meet the desired sensitivity of the accelerometer. Therefore, width (w_m) of the proofmass can be calculated as

$$w_m = \frac{l_m}{\text{Aspect Ratio}}. \quad (15)$$

**Fig. 4** Magnified view of comb structure

The volume and mass of the proofmass is calculated as:

$$V = t_m(l_m \cdot w_m + 2 \cdot N \cdot l_c \cdot w_c) \quad (16)$$

$$m = \rho V, \quad (17)$$

where, ρ is the density of proofmass material, V is the volume of proofmass and m is the mass value of proofmass.

Squeeze-film and Couette-flow are the two damping mechanisms that exist between stator and rotor fingers (Chen 2010). However, Couette-flow damping is much smaller than squeeze-film damping, and its effect is neglected. The damping coefficient for d_1 and d_2 gaps can be modelled by the Eqs. (18, 19) for Hagen-Poiseuille flow as mentioned in (Bao and Yang 2007; Gönenli et al. 2010).

$$b_1 = 7.2\eta_{\text{eff}}t\left(\frac{l}{d_1}\right)^3 \quad (18)$$

$$b_2 = 7.2\eta_{\text{eff}}t\left(\frac{l}{d_2}\right)^3, \quad (19)$$

where, η_{eff} is the effective viscosity, t is the device thickness, l is the overlap length of combs.

Total damping coefficient is given by Eq. (20) and optimized parameters of the accelerometer are given in Table 3.

$$b = b_1 + b_2. \quad (20)$$

Table 3 Optimized parameters of the accelerometer

Parameter	Value
Proofmass dimensions ($l_m \times w_m$)	5778 $\mu\text{m} \times 2311 \mu\text{m}$
Thickness (t)	30 μm
Mass value of proofmass (m)	0.99 mg
Comb dimensions ($l_c \times w_c$)	300 $\mu\text{m} \times 6 \mu\text{m}$
Overlap length (l)	200 μm
Spring dimensions ($l_s \times w_s$)	734 $\mu\text{m} \times 15 \mu\text{m}$
MNEA	0.12 aF/ $\sqrt{\text{Hz}}$
Total noise	63.25 aF
Sensitivity (S)	189.74 fF/g
No. of combs on one side (N)	223
Smaller gap between combs d_1	3.5 μm
Larger gap between combs d_2	10.5 μm
Overall spring constant (k)	87.88 N/m

3 Simulation results

3.1 Modal analysis

The phenomenon with which a system oscillates with large amplitude due to excitation at specific frequencies is called as resonance and those frequencies are called as resonance frequencies. The analysis is carried out to determine the mode or shape with which the accelerometer vibrates and the corresponding modal frequency (Abarca-Jiménez et al. 2014). The dominant mode is along X-axis with a resonant

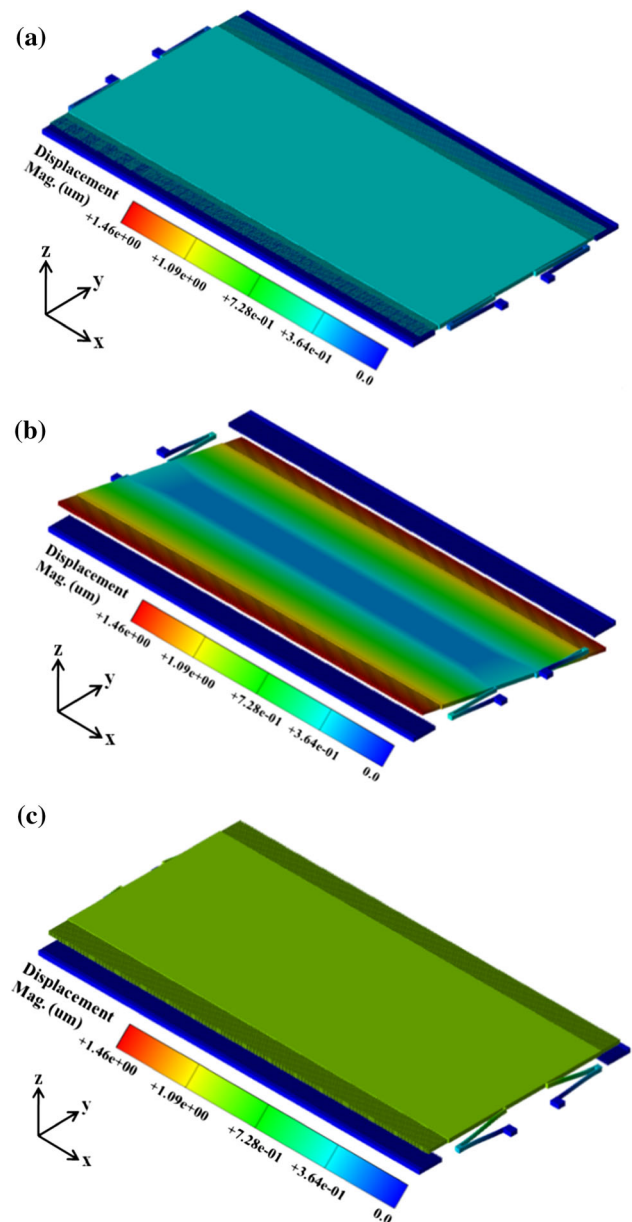


Fig. 5 Resonant modes of accelerometer **a** fundamental mode in X-direction, **b** second mode in torsional across X-direction, **c** third mode in Z-direction

frequency of 1.43 kHz as shown in Fig. 5a. Second mode is torsional across X-axis and third is along Z-axis as shown in Fig. 5b and c, respectively. Table 4 shows the first three modes and their shapes. The analysis is carried out using MEMS+[®].

3.2 Pull-In analysis

The maximum safe voltage that can be applied between proofmass and electrodes is around 80% of the pull-in voltage. Pull-in voltage is the voltage at which the proofmass gets collapsed with the stator fingers, and is given by Eq. (21). A DC-bias greater than pull-in voltage results in spring force to be smaller than the electrostatic force between the combs, and hence, they stick and damage the accelerometer structure. For ensuring safe operation of the accelerometer, the displacement of the proofmass at a typical DC bias should not exceed 1/3 of the gap between stator and rotor finger (Machado da Rocha 2005). The analysis is carried out using MEMS+[®] as shown in Fig. 6.

$$V_{\text{pull-in}} = \sqrt{\frac{8ka_1^3}{27.l.t.N.\epsilon}}. \quad (21)$$

3.3 Harmonic analysis

The analysis is carried out in MEMS+[®] to determine the magnitude and phase response of the accelerometer over a frequency range to check the quality factor and bandwidth of the accelerometer. For an underdamped system, frequency response is given by Eq. (26) as mentioned in (Sinha et al. 2014). Figure 7a shows the frequency and phase response using analytical modelling, Fig. 7b, c shows the frequency response using MEMS+[®] and corresponding phase response using MEMS+[®], respectively. The magnitude of displacement of proofmass is maximum at resonant frequency and the output follows the input in the working range, as depicted in the phase response. Under biasing conditions there exists an electrostatic force between electrodes and Eq. (2) can be rewritten as (Sinha et al. 2014):

Table 4 Modal frequency

S.no	Mode frequency (Hz)	Mode shape
1	1433.43	Along X-axis
2	2477.04	Torsional across X-axis
3	2548.73	Along Z-axis

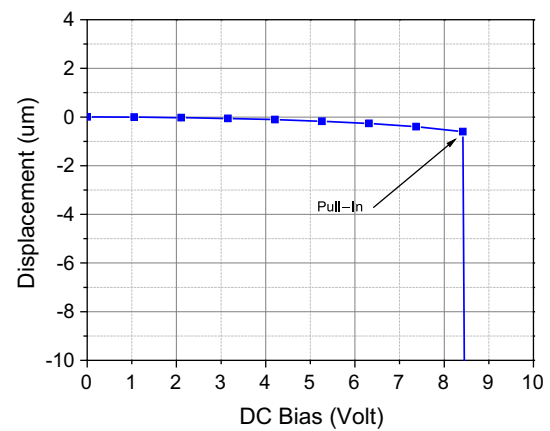


Fig. 6 Pull-in analysis

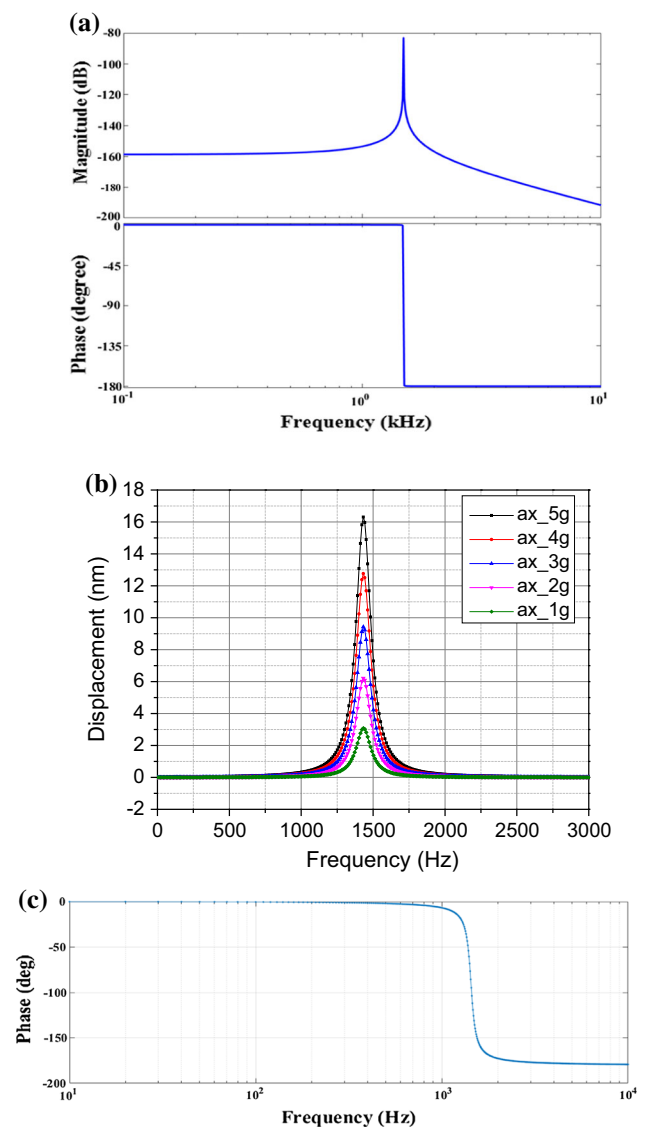


Fig. 7 a frequency and phase response using analytical modelling, b frequency response using MEMS+ 6 for 1 g to 5 g, c phase response using MEMS+

$$m\ddot{x} + b\dot{x} + kx = ma + F_{dc}\left(\frac{x}{d}\right) - F_{ac} \sin \omega t \quad (22)$$

$$F_{dc} = \frac{2.N.\varepsilon.L.t.V_{dc}^2}{d_1^2} \quad (23)$$

$$F_{ac} = \frac{2.N.\varepsilon.L.t.V_{dc}V_o}{d_1^2}. \quad (24)$$

Let,

$$\omega_n = \sqrt{\frac{k}{m}}; Q = \frac{m\omega_n}{b}; Q = \frac{1}{2\zeta};$$

and Normalizing the Eq. (24) as mentioned in [15],

$$\tau = \omega_n t; X = \frac{x}{d}; \hat{a} = \frac{a}{\omega_n^2}; f_{dc} = \frac{F_{dc}}{d\omega_n^2 m}; f_{ac} = \frac{F_{ac}}{d\omega_n^2 m};$$

Equation (24) can now be written as:

$$\frac{d^2 X}{d\tau^2} + 2\zeta \frac{dX}{d\tau} + (1 - f_{dc})X = \hat{a} - f_{ac} \sin \tau. \quad (25)$$

Taking Laplace we get,

$$\frac{\hat{X}(s)}{\hat{a} - f_{ac}} = \frac{1}{(s^2 + 2\zeta s + \tilde{\omega}_r^2)}, \quad (26)$$

where,

$$\tilde{\omega}_r^2 = \omega_n^2(1 - f_{dc}),$$

is the resonant frequency.

3.4 Transient analysis

3.4.1 Transient analysis from a quiet state

A short delay is required for the proofmass to oscillate at its full stroke when the accelerometer is powered on, due to inertial and damping effects. To achieve the steady state, the accelerometer is given sufficient time to oscillate at its

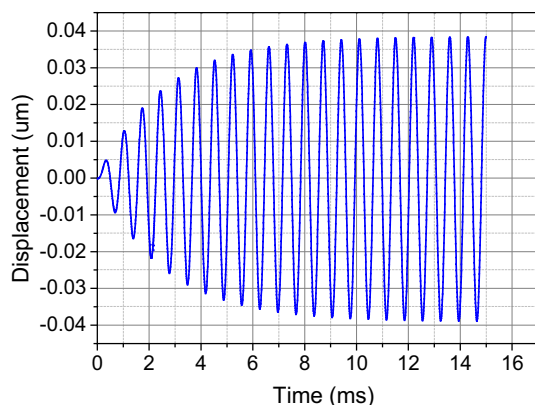


Fig. 8 Transient from quiet state

full stroke before sensing. Figure 8 shows that a time of 10 ms is required for the same.

3.4.2 Transient analysis from a steady state

For the modelled accelerometer, values of all the voltages and positions that result from the frequency analysis can then be used as the starting point for a subsequent transient analysis. The accelerometer is excited with 5 g acceleration from 16 to 31 ms as step input. The analysis shown in Fig. 9 is carried out using MATLAB® and MEMS+®. The negative sign depicts that proof mass is moving in negative X-axis direction. Settling time is ~ 5 ms.

4 System level simulations

The readout circuitry detects the minuscule differential change in capacitance resulting from the displacement of proofmass due to applied acceleration. The concept of Universal Readout IC™ MS3110 is implemented in MATLAB Simulink®, and similar transfer function is used to read the applied acceleration. The full block diagram of readout circuitry consisting of capacitance to voltage converter, demodulator and a low pass filter is shown in Fig. 10.

4.1 Universal Readout IC™ (MS3110)

The Universal Readout IC™ MS3110 is a standard capacitance to voltage converter manufactured by Irvine Sensors having a resolution $4 \text{ aF}/\sqrt{\text{Hz}}$. A single 5 V DC supply is required for its operation. Its features include programmable gain and bandwidth, trimmable DC offset. It consists of an on chip EEPROM for programming specifications. Timing signals are generated internally and

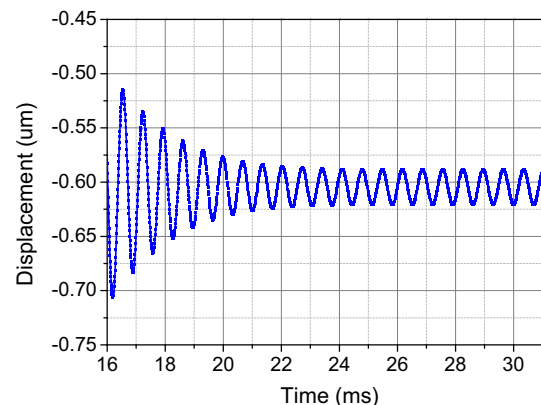


Fig. 9 Transient response using MEMS+®

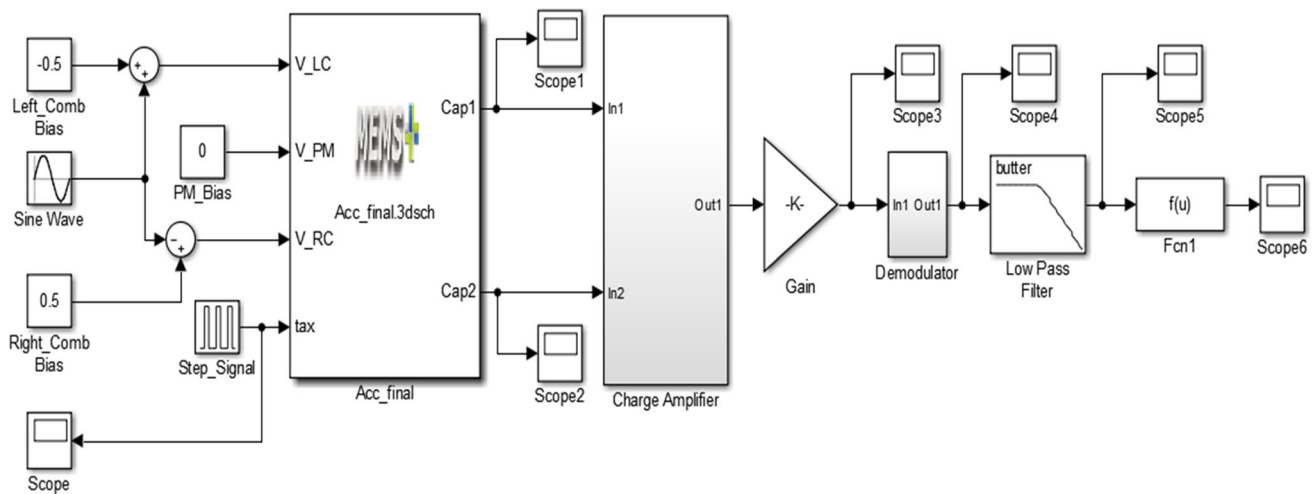


Fig. 10 System level Simulink model of the accelerometer

output voltage ranges from 0.5 to 4 V (Datasheet MUCRI 2004). The transfer function of the IC is given by Eq. (27)

$$V_o = \text{Gain} \times V2P25 \times 1.14 \times \frac{(CS2_T - CS1_T)}{C_F} + 2.25. \quad (27)$$

4.2 Charge amplifier

Figure 11a shows the capacitance formation in the accelerometer. The operation of charge amplifier

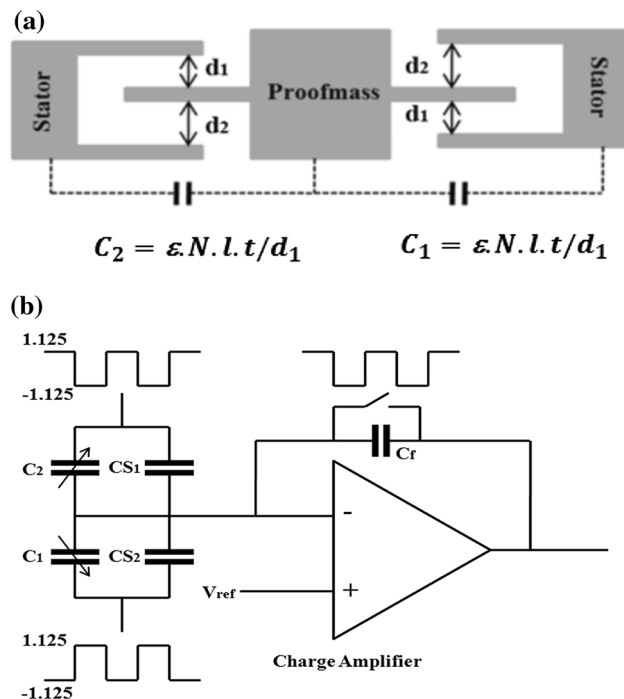


Fig. 11 **a** capacitance formation view at the combs, **b** schematic of charge amplifier

(Fig. 11b) is dependent on the state of switch. Operation of the circuit consists of reset and integration phases that are defined by the closed and open states of the switch, respectively (Yazicioglu 2003). Under equilibrium $C_1 = C_2 = C$ as shown in Fig. 11a. As $d_2 = 3.d_1$, the value of $C_1 = C_2$, are considered only for the small gap capacitors which are larger in value and dominating over the large gap capacitors. The capacitance due to larger gap is neglected. C is nominal capacitance under static conditions. When acceleration is applied, the proofmass displaces and there is a change in capacitance denoted by ΔC (Sharma et al. 2007).

$$C_1 = \frac{\epsilon.N.l.t}{d_1 + x} = \frac{\epsilon.N.l.t}{d_1 \left(1 + \frac{x}{d_1}\right)} \approx \frac{\epsilon.N.l.t}{d_1} \left(1 - \frac{x}{d_1}\right) = C - \Delta C, \quad (28a)$$

$$C_2 = \frac{\epsilon.N.l.t}{d_1 - x} = \frac{\epsilon.N.l.t}{d_1 \left(1 - \frac{x}{d_1}\right)} \approx \frac{\epsilon.N.l.t}{d_1} \left(1 + \frac{x}{d_1}\right) = C + \Delta C, \quad (28b)$$

$$2.\Delta C = C_2 - C_1 = \frac{2.\epsilon.N.l.t}{d_1} \left(\frac{x}{d_1}\right) = 2C \left(\frac{x}{d_1}\right), \quad (28c)$$

where

$$C = \frac{\epsilon.N.l.t}{d_1}$$

and

$$\Delta C = \frac{\epsilon.N.l.t}{d_1^2}.$$

The charge at two different stages is given by Eqs. (29, 30).

$$Q_1 = 1.125(C + \Delta C + CS_1) - 1.125(C - \Delta C + CS_2) \quad (29)$$

$$Q_2 = 1.125(C - \Delta C + CS_2) - 1.125(C + \Delta C + CS_1) + \Delta VC_f. \quad (30)$$

From the charge conservation rule, total charge at two different stages must be equal. Hence $Q_1 = Q_2$, which gives the voltage proportional to change in capacitance given by the Eq. (31).

$$\Delta V = V_{\text{bias}} \left(\frac{2\Delta C + \Delta X}{C_f} \right), \quad (31)$$

where V is the change in output voltage w.r.t V_{ref} , C is the change in capacitance, ΔX is the change in capacitance ($CS_1 - CS_2$) and C_f is the integration capacitance, V_{bias} is the peak to peak voltage of complimentary signals used to modulate capacitances. CS_1 and CS_2 are trimmable capacitors to limit the output in the range of 0.5 to 4 V. Table 5 shows the value of various parameters taken.

4.3 Demodulation and filtering

The output of charge amplifier is modulated by the carrier amplitude and has to be demodulated. A gain block is added to provide gain. Similar pulse is multiplied to modulated wave to get a demodulated change in sensed voltage. The output of the demodulator is filtered with low pass filter with a cut-off frequency 500 Hz to get change in output voltage ΔV_o and is finally added with the reference voltage (2.25 V) using Fcn1 block to get the output voltage V_o .

$$\Delta V_o = V_{\text{bias}} \times \text{Gain} \times \left(\frac{2\Delta C + \Delta X}{C_f} \right) \quad (32)$$

$$V_o = V_{\text{bias}} \times \text{Gain} \times \left(\frac{2\Delta C + \Delta X}{C_f} \right) + V_{\text{ref}}. \quad (33)$$

Table 5 Various parameter values

Parameter	Value
V_{bias}	2.25 V
CS_1	0.633 pF
CS_2	0.608 pF
C_f	3.85 pF
Gain	$2 \times 1.14 = 2.28$

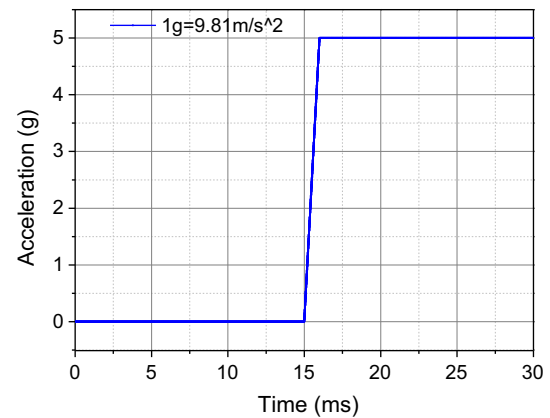


Fig. 12 Step input signal

5 Results and discussion

The accelerometer is subjected to the acceleration of 5 g as step input at 15 ms with rise time of ~ 1 ms as shown in Fig. 12. The step input governs the steady state behaviour of the system.

Figures 13 and 14 show the capacitance signals observed at the output of the accelerometer. Initially, the accelerometer is oscillating at its full stroke and nominal capacitance is observed at both the outputs. When the step input applied, a differential change in capacitance is observed, which implies that C_1 increases and C_2 decreases or vice versa. Further, these signals are appropriately processed to get output in terms of voltage as shown in Fig. 15. The underdamped behaviour of the system is also verified from the graphs.

Since real world signals are dynamic in nature, the dynamic behaviour of the accelerometer is tested using sinusoidal signal of 10 Hz and 100 Hz. Figures 16 and 17 show the sinusoidal input signal given to the accelerometer and corresponding output. The turn-on time of the accelerometer is ~ 0.7 ms.

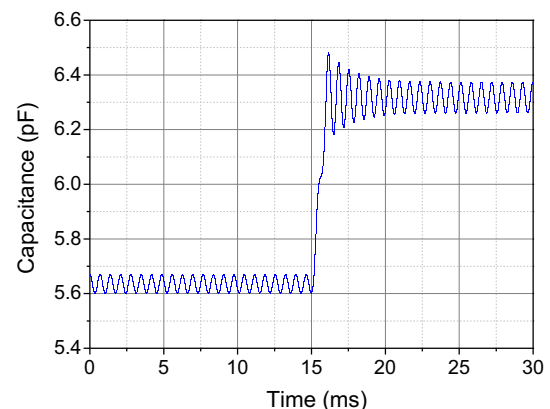


Fig. 13 Sense capacitance 1 for step input signal

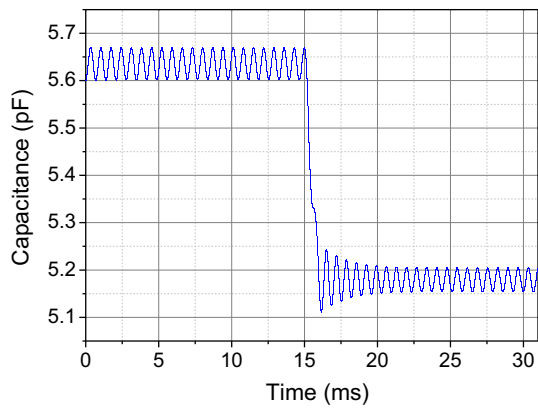


Fig. 14 Sense capacitance 2 for step input signal

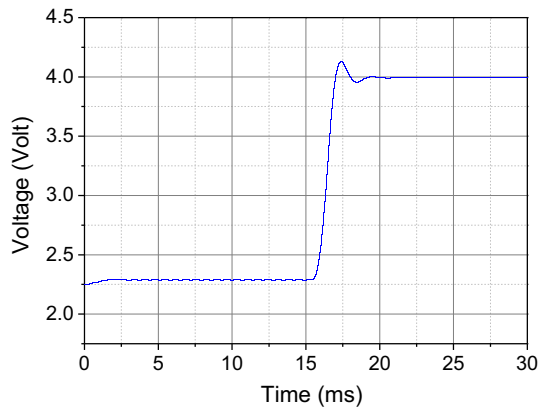


Fig. 15 Output voltage for step input signal

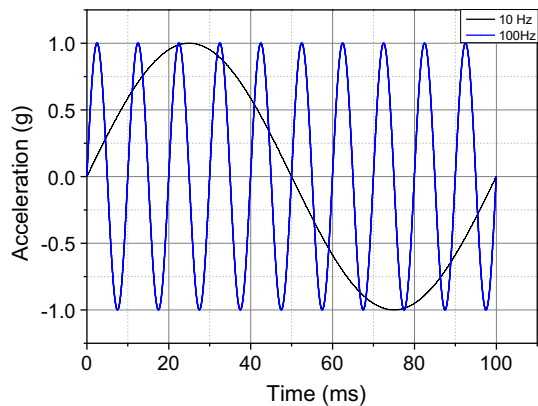


Fig. 16 Sinusoidal input signal

Figures 18, 19 and 20 show the various sensitivity results for all the 3-axis. Maximum magnitude occurs for the acceleration applied along sense axis (X-axis) whereas magnitude along cross-axis (Y-axis and Z-axis) is negligible and the corresponding sensitivities are shown in Table 6. The cross-axis mechanical sensitivity is seven orders of magnitude less than dominant axis sensitivity and cross axis electrical sensitivity is almost 0. The analysis are

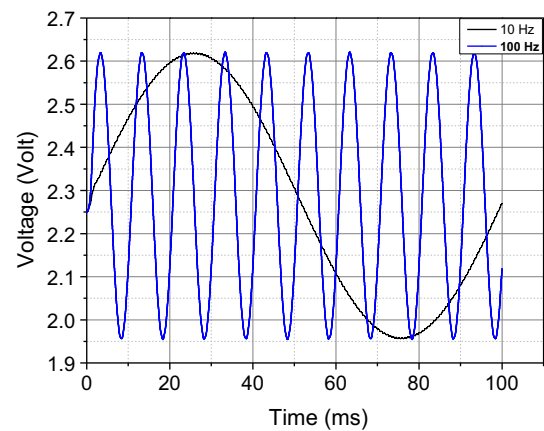


Fig. 17 Output voltage for sinusoidal input signal

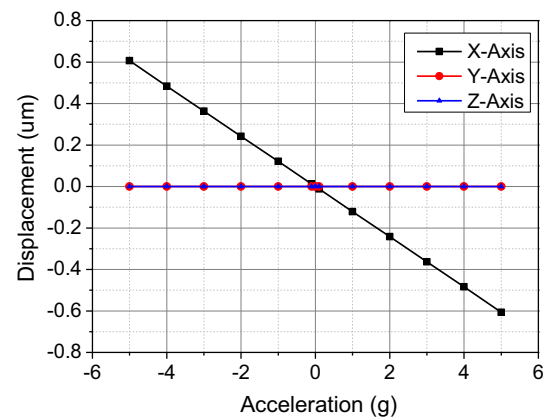


Fig. 18 Displacement vs. acceleration

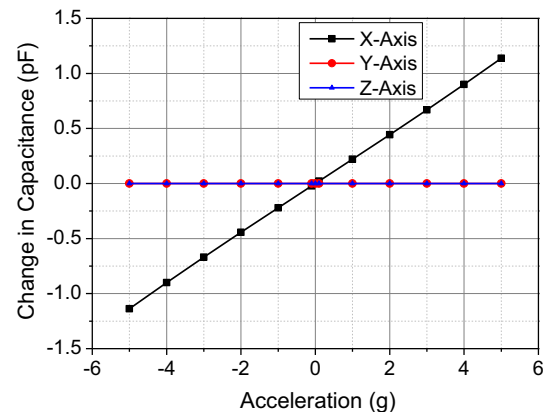


Fig. 19 Change in capacitance vs. acceleration

carried out in MEMS⁺ and MATLAB Simulink[®] and are helpful in determining the output voltage for a given acceleration input.

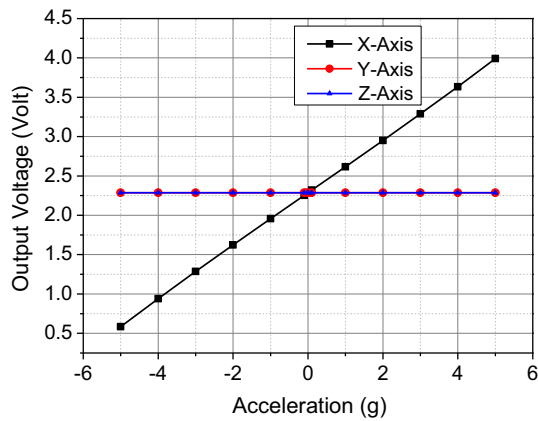


Fig. 20 Output voltage vs. acceleration

Table 7 Comparison between analytical and simulation results

Parameter	Calculated value	Simulated value
Natural frequency (f_n)	1.5 kHz	1.43 kHz
Electrical sensitivity	189 fF/g	225 fF/g
Mechanical sensitivity	0.11 $\mu\text{m/g}$	0.12 $\mu\text{m/g}$
Pull-in voltage	6.9 V	8.43 V
Resolution	1 mg	1 mg
Operating bandwidth	100 Hz	100 Hz

5.1 Cross-axis sensitivity

Each axis is associated with two cross-axis sensitivities: X : S_{xy}, S_{xz} ; Y : S_{yx}, S_{yz} ; Z : S_{zx}, S_{zy} .

The first subscript represents the sensing axis and second represents the off-axis direction. It can be measured as percentage of sensitivity as stated in Eqs. (34, 35).

$$S_{x\text{cross}} = \frac{S_{xy}}{S_x} \times 100 \quad (34)$$

Table 6 Sensitivities analysis

Sensitivity	Displacement sensitivity	Capacitive sensitivity	Voltage sensitivity
S_x	0.121 $\mu\text{m/g}$	225 fF/g	0.34 V/g
S_{xy}	$2.3852 \times 10^{-8} \mu\text{m/g}$	≈ 0	≈ 0
S_{xz}	$1.42167 \times 10^{-11} \mu\text{m/g}$	≈ 0	≈ 0

$$S_{x\text{cross}} = \frac{S_{xz}}{S_x} \times 100. \quad (35)$$

6 Comparison between analytical and simulation results

The comparison between analytically evaluated results and those obtained by simulation are outlined in Table 7. A slight decrease in resonance frequency and increase in sensitivity is observed in simulation results due to fringing field and biasing effects, as these effects are ignored in the analytical calculations. As shown in Fig. 10a; pull-in voltage is found to be high, because one rotor finger is influenced by two stator fingers during simulation in comparison to the pull-in voltage calculated analytically in which only one stator and one rotor finger is considered. Therefore, on sweeping DC bias, both stator fingers are driven by same bias. The force acting between stator and rotor where gap between them is d_1 , is dominant but resultant force acting on the proofmass decreases because of gap d_2 . Hence, overall pull-in voltage in simulation is more in comparison to analytically calculated value.

7 Conclusions

In this paper, design, analytical modelling and system level simulations of DRIE-based accelerometer have been presented. The accelerometer shows good linearity and high sensitivity with very low cross-axis sensitivity in the operating range. The simulation results show a close proximity with the analytically calculated results. A voltage sensitivity of 0.34 mV/g has been achieved by taking voltage range constraints of MS3110. The designed accelerometer can be fabricated using DRIE-based SOI-MUMP process.

Acknowledgements The authors would like to acknowledge the Director, CSIR-CEERI, Pilani for his generous support. We are thankful to all the members and technical staff of Process Technology Group (Smart Sensors Area) for their help and motivation. Financial support from CSIR, India is gratefully acknowledged.

References

- Abarca-Jiménez GS, Reyes-Barranca MA, Mendoza-Acevedo S, Munguia-Cervantes JE, Alemán-Arce MA (2014) Modal analysis of a structure used as a capacitive MEMS accelerometer sensor. In: 11th international conference on electrical engineering, computing science and automatic control (CCE) IEEE, pp 1–4
- Bais B, Majlis BY (2008) Low-g area-changed MEMS accelerometer using bulk silicon technique. *Am J Appl Sci* 5(6):626–632
- Bao M, Yang H (2007) Squeeze film air damping in MEMS. *Sens Actuators A* 136(1):3–27
- Chen JY (2010) Single-and dual-axis lateral capacitive accelerometers based on CMOS-MEMS technology. Master's thesis, University of Oslo
- Datasheet MUCRI (2004) MS3110 Universal Capacitive Readout™ IC. MicroSensors, Inc., 3001 Redhill Avenue, Costa Mesa, CA 92626
- Edalatfar F, Yaghootkar B, Qureshi AQA, Azimi S, Bahreyni B (2016) Design, fabrication and characterization of a high performance MEMS accelerometer. In: *SENSORS 2016*, IEEE, 30 Oct–3 Nov 2016, Orlando, FL, USA, pp 1–3
- Finkbeiner S (2013) MEMS for automotive and consumer electronics. In: *Proceedings of the ESSCIRC (ESSCIRC)*, IEEE, 16–20 Sept 2013, Bucharest, Romania, pp 9–14
- Freescale Semiconductor (2007) Accelerometer terminology guide. Sensors, Peterborough
- Gönenli İE, Çelik-Butler Z, Butler DP (2010) MEMS accelerometers on polyimides for failure assessment in aerospace systems. In: *Sensors*, 2010, IEEE, 1–4 Nov 2010, Kona, HI, USA, pp 1211–1215
- Kannan A (2008) Design and modeling of a MEMS-based accelerometer with pull in analysis. Doctoral dissertation, University of British Columbia
- Machado da Rocha LA (2005) Dynamics and nonlinearities of the electro-mechanical coupling in inertial MEMS. Doctoral dissertation TU Delft, Delft
- Mistry KK, Swamy KBM, Sen S (2010) Design of an SOI-MEMS high resolution capacitive type single axis accelerometer. *Microsyst Technol* 16(12):2057–2066
- Mukhiya R, Gopal R, Pant BD, Khanna VK, Bhattacharyya TK (2015) Design, modeling and fem-based simulations of a 1-dof MEMS bulk micromachined piezoresistive accelerometer. *Microsyst Technol* 21(10):2241–2258
- Qu H (2006) Development of DRIE CMOS-MEMS process and integrated accelerometers. Doctoral dissertation, University of Florida
- Senturia SD (2001) *Microsystem design*. Springer, New York
- Sharma K, Macwan I, Zhang L, Hmurcik LV, Xiong X (2007) Design optimization of MEMS comb accelerometer. ASEE. http://www.asee.org/documents/zones/zone1/2008/student/ASEE12008_0050_paper.pdf
- Sinha S, Shakya S, Mukhiya R, Gopal R, Pant BD (2014) Design and simulation of MEMS differential capacitive accelerometer. In: *Proceeding of ISSS international conference on smart materials, structures and systems*, July 8–11, 2014, Bangalore, India
- Van Spengen WM (2003) MEMS reliability from a failure mechanisms perspective. *Microelectron Reliab* 43(7):1049–1060
- Yazdi N, Ayazi F, Najafi K (1998) Micromachined inertial sensors. *Proc IEEE* 86(8):1640–1659
- Yazicioğlu RF (2003) Surface micromachined capacitive accelerometers using MEMS technology. Doctoral dissertation, Middle East Technical University

Publisher's Note Springer Nature remains neutral with regard to jurisdictional claims in published maps and institutional affiliations.